
Learning Time-Varying Multi-Region Communications via Scalable Markovian Gaussian Processes

Weihan Li¹, Yule Wang¹, Chengrui Li¹, Anqi Wu¹,

¹School of Computational Science & Engineering,
Georgia Institute of Technology, Atlanta, GA 30332,
weihanli@gatech.edu, yulewang@gatech.edu,
cnlichengrui@gatech.edu, anqiwu@gatech.edu

Abstract

Understanding and constructing brain communications that capture dynamic communications across multiple regions is fundamental to modern system neuroscience, yet current methods struggle to find time-varying region-level communications or scale to large neural datasets with long recording durations. We present a novel framework using Markovian Gaussian Processes to learn brain communications with time-varying temporal delays from multi-region neural recordings, named Adaptive Delay Model (ADM). Our method combines Gaussian Processes with State Space Models and employs parallel scan inference algorithms, enabling efficient scaling to large datasets while identifying concurrent communication patterns that evolve over time. This time-varying approach captures how brain region interactions shift dynamically during cognitive processes. Validated on synthetic and multi-region neural recordings datasets, our approach discovers both the directionality and temporal dynamics of neural communication. This work advances our understanding of distributed neural computation and provides a scalable tool for analyzing dynamic brain networks.

1 Introduction

Modern system neuroscience faces a significant challenge in discovering communication patterns that capture dynamic interactions across multiple regions. Understanding these time-varying communications has become increasingly critical with the advent of advanced recording technologies that enable simultaneous measurement of neural activity across numerous brain areas with unprecedented temporal and spatial resolution [Steinmetz et al. \[2021\]](#); [Siegle et al. \[2021\]](#). These large-scale neural recordings necessitate computational methods capable of uncovering and characterizing the dynamic nature of neural communication within the brain.

Latent representations offer a promising approach to building time-varying multi-region communications. In the brain, communication patterns between brain regions manifest at varying temporal scales: some regions exhibit fast, synchronous interactions with short delays, indicative of strong functional coupling, while others display slower interactions with longer delays, reflecting more indirect relationships. Such communications provide a framework for understanding how these diverse communication patterns evolve over time, capturing both feedforward and feedback pathways that may shift during different cognitive states [Lillicrap et al. \[2020\]](#).

Current computational approaches for modeling multi-region communications can be broadly categorized into non-delay models and delay models. Non-delay models, such as mp-srSLDS [Glaser et al. \[2020\]](#) and MR-SDS [Karniol-Tambour et al.](#), do not explicitly incorporate temporal delays when

capturing latent dynamics across regions. As a result, they can only learn the directional information of communications. Delay models, including DLAG [Gokcen et al. \[2022\]](#), m-DLAG [Gokcen et al. \[2024a\]](#), their approximated versions [Gokcen et al. \[2024b\]](#), and MRM-GP [Li et al. \[2024\]](#), introduce mechanisms to learn temporal delays between pairs of communications. Learning delays provides not only directional information but also insights into relative communication speeds, which can help assess the strength of functional coupling between brain regions.

Although these methods have shown potential in capturing inter-region brain communications, delay models, such as DLAG and its variants, do not account for the dynamic nature of multi-region communication. They fail to model time-varying temporal dependencies and communication patterns, which are crucial for understanding neural processing. Non-delay models, such as MR-SDS and mp-srSLDS, introduce dynamic message flow among regions but don't model delays between communications and assume a single communication subspace, meaning they cannot capture concurrent communications over different subspaces.

MRM-GP is a specific case that integrates a Gaussian Process (GP) with a State Space Model (SSM), making it a delay model with discrete changing of phase delays. MRM-GP has two key limitations: (1) it only supports kernels that are separable across spatial and temporal domains, restricting its applicability in the frequency domain by learning phase delays, whereas temporal delays are more generalizable for neuroscience applications; (2) it assumes that the delays across all communication subspaces across regions change synchronously with hidden state transition. However, this assumption does not reflect the true brain mechanism, where different communication pathways between regions can operate asynchronously.

In terms of computational efficiency, DLAG and mDLAG, which are GP-based methods, incur an $O(T^3)$ computational cost, where T is the number of time samples, making them challenging to scale. Approximated GP and SSM-based methods, such as MRM-GP, MR-SDS, and mp-srSLDS, reduce the cost to $O(T)$. However, they rely on sequential inference, which remains inefficient for large neural datasets with long recording durations. Moreover, the reliance on discrete hidden states, e.g., MRM-GP, introduces inefficiencies during inference.

To address these limitations, we propose the Adaptive Delay Model (ADM). It falls within the family of Markovian Gaussian process-based delay models [Zhao \[2021\]](#); [Li et al. \[2024\]](#), but incorporates a continuous time-varying temporal delay. Thus unlike static communication models commonly used in neuroscience, ADM can accommodate communication patterns with varying temporal characteristics, offering a more flexible and biologically relevant framework.

Markovian Gaussian Process (Markovian GP) models integrate the expressive power of GPs with the computational efficiency of SSMs, facilitating scalable analysis of large-scale neural recordings while discovering multiple evolving communication patterns. However, existing Markovian GP approaches either depend on single-output kernels or impose separability constraints on spatial and temporal kernels [Solin et al. \[2016\]](#); [Loper et al. \[2021\]](#); [Li et al. \[2024\]](#). In this paper, we introduce a novel, universal connection between arbitrary temporally stationary GPs and SSMs, making the framework highly flexible and broadly applicable to various neuroscience problems.

Additionally, we apply an advanced inference method for Markovian GP, leveraging parallel scan algorithms [Blelloch \[1990\]](#); [Särkkä & García-Fernández \[2020\]](#) to significantly accelerate computation and reducing complexity to $O(\log T)$. This approach enables efficient analysis of long-duration recordings while capturing dynamic communication patterns.

We validate our model using neural recordings from multiple regions of the brain during visual processing tasks [Semedo et al. \[2019\]](#); [Siegle et al. \[2021\]](#). Our results demonstrate the method's capability to uncover how information flow patterns dynamically change across multi-region networks, offering new insights into the temporal organization of large-scale neural circuits and advancing our understanding of distributed neural computation.

In summary, the key contributions of our work are:

- We establish a universal connection between arbitrary temporally stationary GPs and SSMs, which has broader implications for other domains where computational efficiency is a priority.
- Our model discovers time-varying multi-region communications from latent representations of neural recordings without introducing additional discrete hidden states in the SSM.

- We propose a scalable method for analyzing multi-region communications in large-scale neural data with $O(\log T)$ complexity.

2 Method

We begin by demonstrating how a Gaussian Process (GP) with a Factor Analysis (FA) model can be used to capture static brain communication across regions (Section 2.1). Next, we establish a universal connection between a GP and a State Space Model (SSM), referred to as the Markovian Gaussian Process (Section 2.2). Finally, we illustrate how time-varying brain communication can be modeled (Section 2.3).

2.1 Gaussian Process Factor Analysis for Brain Communications

The Gaussian Process Factor Analysis (GPFA) for modeling brain communication employs the multi-output Squared Exponential (MOSE) kernel [Gokcen et al. \[2022\]](#):

$$\mathbf{K}_{ij}(\tau) = \exp\left(-\frac{(\tau + \theta_{ij})^2}{2l^2}\right), \quad (1)$$

where i, j represent two brain regions, $\tau = t - t'$ is the time difference, θ_{ij} is the temporal delay between regions i and j , and l is the length scale shared across all regions. This MOSE kernel allows the identification of temporal delays that characterize communication dynamics across regions.

Our goal is to learn MN latent variables, $\mathbf{x} \in \mathbb{R}^{MN \times T}$, from neural recordings $\mathbf{y} \in \mathbb{R}^{D \times T}$ across N regions. Each region is associated with M latent variables.

A typical assumption for \mathbf{x} is to decompose it into two components: across-region variables and within-region variables [Gokcen et al. \[2022\]](#); [Li et al. \[2024\]](#). The across-region variables, $\mathbf{x}^a \in \mathbb{R}^{m_a N \times T}$, capture shared neural activity that reflects communication between brain regions. These variables exhibit the similar dynamics across regions, differing only in temporal delays. The within-region variables, $\mathbf{x}^w \in \mathbb{R}^{m_w N \times T}$, represent neural activity unique to individual regions and are independent of other regions. Together, these components form the latent representation of neural recordings, $\mathbf{x} = [\mathbf{x}^a, \mathbf{x}^w]$, where $m_a + m_w = M$. The relationship between \mathbf{y} and \mathbf{x} is then modeled using a Factor Analysis (FA) model:

$$\mathbf{y} = \mathbf{Cx} + d + \epsilon, \quad (2)$$

where $\mathbf{C} \in \mathbb{R}^{D \times MN}$ is a block-diagonal matrix $\mathbf{C} = \text{diag}\{\mathbf{C}^1, \dots, \mathbf{C}^N\}$, with each \mathbf{C}^i representing the mapping from region i 's latent variable to its neural recordings. Additionally, $d \in \mathbb{R}^{D \times 1}$ is a bias term, and $\epsilon \sim \mathcal{N}(0, \mathbf{V})$ represents Gaussian noise with diagonal covariance $\mathbf{V} \in \mathbb{R}^{D \times D}$.

The across-region variables \mathbf{x}^a are designed to capture communication patterns among regions. For the m -th group of across-region variables, $\mathbf{x}_m^a \in \mathbb{R}^{N \times T}$, the activity from each region exhibits spatial correlations with the $N - 1$ other regions. These variables are modeled as a Gaussian Process (GP) with the MOSE kernel, which captures the temporal delay characteristics of across-region communication.

On the other hand, the m -th group of within-region variables $\mathbf{x}_m^w \in \mathbb{R}^{N \times T}$, representing region-specific activity, is modeled independently across regions using a single-output Squared Exponential (SE) kernel:

$$\mathbf{K}^{\text{single}}(\tau) = \exp\left(-\frac{\tau^2}{2l^2}\right). \quad (3)$$

Additionally, independence is assumed across different groups of both the across-region and within-region variables, with each group m governed by distinct kernel parameters.

By explicitly separating the across-region and within-region latent variables, this framework offers a clear representation of across-region communication and region-specific dynamics, enabling a more interpretable analysis of multi-region neural recordings.

2.2 Connect Gaussian Process with State Space Model

We develop a novel universal connection between arbitrary temporally stationary GPs and SSMs, enabling us to efficiently model both across- and within-region dynamics.

Gaussian Process and State-Space Approximation. The m -th group of across-region variables, $\mathbf{x}_m^a \in \mathbb{R}^{N \times T}$ are modeled as a GP with MOSE kernel:

$$\mathcal{GP}(0, \begin{bmatrix} \mathbf{K}(0) & \mathbf{K}(-1) & \dots & \mathbf{K}(-T+1) \\ \mathbf{K}(1) & \mathbf{K}(0) & \dots & \mathbf{K}(-T+2) \\ \vdots & \vdots & \ddots & \vdots \\ \mathbf{K}(T-1) & \mathbf{K}(T-2) & \dots & \mathbf{K}(0) \end{bmatrix}), \quad (4)$$

where each $\mathbf{K}(\tau) \in \mathbb{R}^{N \times N}$ is a MOSE kernel in Eq. 1 with an interval τ over N brain regions. Our goal is to find a state-space approximation of \mathbf{x}_m^a , which follows a Multi-Order SSM structure:

$$\mathbf{x}_{m,t}^a = \sum_{p=1}^P \mathbf{A}_p \mathbf{x}_{m,t-p}^a + \mathbf{q}_t, \quad \mathbf{q}_t \sim \mathcal{N}(0, \mathbf{Q}), \quad (5)$$

where P represents the number of orders, $\mathbf{A}_1, \dots, \mathbf{A}_P \in \mathbb{R}^{N \times N}$ are the transition matrices, and $\mathbf{Q} \in \mathbb{R}^{N \times N}$ is the process noise matrix.

Determining an State Space Model using Kernels. To estimate transition matrices and measurement using \mathbf{x}_m^a , we can consider the SSM in Eq. 5 as a regression model [Neumaier & Schneider \[2001\]](#):

$$\mathbf{x}_{m,t}^a = \mathbf{G} \mathbf{v}_t + \mathbf{q}_t, \quad \mathbf{q}_t \sim \mathcal{N}(0, \mathbf{Q}), \quad (6)$$

where $\mathbf{G} \in \mathbb{R}^{N \times NP}$ is the regression coefficient and $\mathbf{v}_t \in \mathbb{R}^{NP \times 1}$ is the predictor:

$$\begin{aligned} \mathbf{G} &= [\mathbf{A}_P, \mathbf{A}_{P-1}, \dots, \mathbf{A}_1], \\ \mathbf{v}_t &= [\mathbf{x}_{m,t-p}^{a,\top}, \mathbf{x}_{m,t-P+1}^{a,\top}, \dots, \mathbf{x}_{m,t-1}^{a,\top}]^\top. \end{aligned} \quad (7)$$

Our ultimate goal is to use $\mathbf{K}(\tau)$ to represent \mathbf{G} and \mathbf{Q} . First, we can represent \mathbf{G} and \mathbf{Q} as functions of \mathbf{x}_m^a . Concretely, given T samples, $\mathbf{x}_{m,1}^a, \dots, \mathbf{x}_{m,T}^a$, we define predictor matrix as $\mathbf{V} = [\mathbf{v}_{P+1}, \dots, \mathbf{v}_T]^\top \in \mathbb{R}^{NP \times (T-P)}$ and target observation matrix as $\mathbf{W} = [\mathbf{x}_{m,P+1}^a, \dots, \mathbf{x}_{m,T}^a] \in \mathbb{R}^{N \times (T-P)}$.

Then, we can represent the regression model in Eq. 6 in the matrix form: $\mathbf{W} = \mathbf{G} \mathbf{V} + \mathbf{R}$, where \mathbf{R} is the residual matrix. By doing so, we can estimate coefficient matrix \mathbf{G} and the process noise matrix \mathbf{Q} by least squares estimation:

$$\mathbf{G} = \mathbf{W} \mathbf{V}^\top (\mathbf{V} \mathbf{V}^\top)^{-1}, \quad \mathbf{Q} = \frac{\mathbf{R} \mathbf{R}^\top}{T - P - 1}, \quad (8)$$

where $\mathbf{R} = \mathbf{W} - \mathbf{G} \mathbf{V}$ denotes an estimate of the residual matrix, and its covariance is an estimate of process noise matrix \mathbf{Q} . Now, if we can represent $\mathbf{W} \mathbf{V}^\top$, $\mathbf{W} \mathbf{W}^\top$, and $\mathbf{V} \mathbf{V}^\top$ with $\mathbf{K}(\tau)$, we will achieve the ultimate goal.

Since each sample $\mathbf{x}_{m,t}^a$ in \mathbf{V} and \mathbf{W} is modeled as a sample in the GP in Eq. 4. We can represent $\mathbf{V} \mathbf{V}^\top \in \mathbb{R}^{NP \times NP}$, $\mathbf{W} \mathbf{V}^\top \in \mathbb{R}^{N \times NP}$ and $\mathbf{W} \mathbf{W}^\top \in \mathbb{R}^{N \times N}$ using $\mathbf{K}(\tau)$ as (full derivations see [Appendix A](#)):

$$\begin{aligned} \mathbf{V} \mathbf{V}^\top &\propto \begin{bmatrix} \mathbf{K}(0) & \mathbf{K}(-1) & \dots & \mathbf{K}(-P+1) \\ \mathbf{K}(1) & \mathbf{K}(0) & \dots & \mathbf{K}(-P+2) \\ \vdots & \vdots & \ddots & \vdots \\ \mathbf{K}(P-1) & \mathbf{K}(P-2) & \dots & \mathbf{K}(0) \end{bmatrix}, \\ \mathbf{W} \mathbf{V}^\top &\propto [\mathbf{K}(P) \quad \mathbf{K}(P-1) \dots \quad \mathbf{K}(1)], \\ \mathbf{W} \mathbf{W}^\top &\propto \mathbf{K}(0). \end{aligned} \quad (9)$$

Notably, each $\mathbf{K}(\tau) \in \mathbb{R}^{N \times N}$, where $\tau \in [-P+1, P-1]$, depends only on the feature dimension N of the observations and can be efficiently computed using the stationary kernel function employed in the GP. Furthermore, $\mathbf{K}(\tau)$ can represent any stationary temporal kernel, establishing a universal connection between GPs and SSMs. We apply this universal conversion to various kernels in GP regression task, see [Appendix D](#) for details.

Markovian Across-region Communications. Now, the transition matrices and the measurement matrix in Eq. 5 are uniquely determined by the kernel functions of GP by Eq. 8 and Eq. 9. Moreover, we can rewrite the SSM in Eq. 5 to an SSM with a Markovian structure, resulting in a Markovian Gaussian Process (Markovian GP) Zhao [2021]:

$$\begin{aligned}\hat{x}_{m,t}^a &= \hat{\mathbf{A}}\hat{x}_{m,t-1}^a + \mathbf{q}_t, \quad \mathbf{q}_t \sim \mathcal{N}(0, \hat{\mathbf{Q}}), \\ \mathbf{x}_{m,t}^a &= \mathbf{H}\hat{x}_{m,t}^a,\end{aligned}\tag{10}$$

where $\mathbf{H} \in \mathbb{R}^{N \times NP}$ denotes a mask matrix, $\hat{\mathbf{A}} \in \mathbb{R}^{NP \times NP}$ is structured as a controllable canonical form Grewal & Andrews [2014] and ones are added to $\hat{\mathbf{Q}} \in \mathbb{R}^{NP \times NP}$ so it matches the shape of $\hat{\mathbf{A}}$:

$$\begin{aligned}\hat{\mathbf{A}} &= \begin{bmatrix} \mathbf{A}_1 & \mathbf{A}_2 & \dots & \mathbf{A}_{P-1} & \mathbf{A}_P \\ \mathbf{I}_N & 0 & \dots & 0 & 0 \\ 0 & \mathbf{I}_N & \dots & 0 & 0 \\ 0 & 0 & \ddots & 0 & 0 \\ 0 & 0 & \dots & \mathbf{I}_N & 0 \end{bmatrix}, \\ \hat{\mathbf{Q}} &= \begin{bmatrix} \mathbf{Q} & 0 \\ 0 & \mathbf{I}_{N(P-1)} \end{bmatrix}, \quad \mathbf{H} = [\mathbf{I}_N \quad 0],\end{aligned}\tag{11}$$

with $\mathbf{I}_N \in \mathbb{R}^{N \times N}$ being an identity matrix. Notably, although we use a Markovian structure to represent a stationary GP, our method still incorporates information from multiple orders.

Markovian Within-region Neural Activity. Similarly, the state-space approximation of the m -th group of within-region variables, $\mathbf{x}_m^w \in \mathbb{R}^{N \times T}$, can be seen as a specific case of across-region variables. In this case, each dimension, $\mathbf{x}_{m,n}^w \in \mathbb{R}^{T \times 1}$, is independently modeled as a Markovian GP with a scalar single-output SE kernel (Eq. 3).

2.3 Time-Varying Brain Communications

Since the SSM in Eq. 10 follows a discrete structure, we can extend it to incorporate time-varying transition and process noise matrices as follows:

$$\begin{aligned}\hat{x}_{m,t}^a &= \hat{\mathbf{A}}_t \hat{x}_{m,t-1}^a + \mathbf{q}_t, \quad \mathbf{q}_t \sim \mathcal{N}(0, \hat{\mathbf{Q}}_t), \\ \mathbf{x}_{m,t}^a &= \mathbf{H}\hat{x}_{m,t}^a.\end{aligned}\tag{12}$$

This formulation introduces a time-varying MOSE kernel, where the temporal delay parameter $\theta_{ij,t}$ evolves over time. In other words, at each time step t , we construct a Markovian GP (or SSM) as described in Eq. 10, conditioned on the MOSE kernel specific to that time t . Additionally, the length scale parameter l remains constant over time thus constraining the freedom of each $\hat{\mathbf{A}}_t$.

This approach enables the model to learn time-varying temporal delays, effectively capturing the dynamics of multi-region brain communications. Compared to modeling time-varying phase delays using hidden discrete states Li et al. [2024], our method is more flexible, as it does not assume that each group of across-region communications, \mathbf{x}_m^a , undergoes simultaneous delay changes during state transitions.

Importantly, this computation can be efficiently performed in vectorized form across all T time steps, ensuring minimal impact on overall computational efficiency. In the FA model, the projection matrix $\mathbf{C} \in \mathbb{R}^{D \times MN}$, the bias term $d \in \mathbb{R}^{D \times 1}$, and the observation Gaussian noise $\epsilon \in \mathbb{R}^{D \times 1}$ remain time-invariant.

3 Inference

Now, having established the connection between the m -th group of across-region communications and within-region neural activity to the Markovian GP (or SSM), as described in Eq. 12, the next step is to efficiently learn the latent variables and model parameters.

Our model, ADM, formulated as an SSM, offers a significant advantage: it can learn the parameters using either a sequential estimation method with complexity $O(T)$ or a parallel computation method with complexity $O(\log T)$. On modern hardware, the parallel approach is consistently faster due to its efficient utilization of computational resources.

Parameter Settings The model parameters, denoted as Θ , include the kernel parameters $\theta_{ij,t}^k$ and l^k from each latent dimension k , which define the transition matrix $\hat{\mathbf{A}}_t$ and the process noise covariance matrix $\hat{\mathbf{Q}}_t$ for each across- or within-region latent group. Additionally, the Factor Analysis (FA) parameters include the projection matrix \mathbf{C} , the bias term d , and the diagonal matrix \mathbf{V} . The model also has a hyperparameter P , representing the order of the autoregressive process. To better understand the effect of different P values, we generate samples from our model for various P values, as shown in Appendix C.

Parallel Scan Kalman EM Algorithm Given neural recordings $\mathbf{y} \in \mathbb{R}^{D \times T}$, our goal is to estimate the latent brain communications $\mathbf{x} \in \mathbb{R}^{MN \times T}$ along with the model parameters Θ . To achieve this, we use the parallel scan-based Kalman Expectation-Maximization (EM) inference algorithm Särkkä & García-Fernández [2020], which introduces a parallel scan version of the Kalman Filter and Smoother. Specifically, in the E-step, we apply the parallel Kalman Filter and Smoother to infer the latent variables and expected log-likelihood. In the M-step, we update the kernel parameters using gradient descent and optimize the Factor Analysis (FA) parameters through closed-form linear regression. See Appendix B for details.

The objective of the Kalman Filter is to compute the posterior density $p(\mathbf{x}_t | \mathbf{y}_{0:t})$, given the neural data up to time step t , while the Kalman Smoother computes the posterior density $p(\mathbf{x}_t | \mathbf{y}_{0:T})$ for all time steps. Traditionally, both filtering and smoothing are computed in $O(T)$ time using sequential updates. However, sequential computation is often inefficient compared to parallel computation, particularly on modern hardware architectures.

To address this inefficiency, Särkkä & García-Fernández [2020] demonstrates that the sequential updates of the Kalman Filter and Smoother can be reformulated as an associative operator, enabling the use of the parallel scan algorithm Blelloch [1990]. Consequently, the time complexity and memory cost of our model are given by:

$$\text{Time complexity: } O(MN^3P^3 \log T), \quad (13)$$

$$\text{Memory complexity: } O(MN^2P^2T), \quad (14)$$

where N is the number of regions, M is the group number of across- and within-region latent dynamics, and P is the SSM order in Eq. 5. The cubic cost arises from Eq. 8. However, as we will show in the experimental section, the order parameter P and N can be significantly smaller compared to T while still achieving strong generative and inference performance. Thus, the cubic cost does not pose a major computational bottleneck.

4 Experiment

Datasets. We evaluate our model on three datasets.

- **Synthetic Data:** We generate synthetic data that incorporate both across-region communications and within-region neural activities, along with time-varying temporal delays, to simulate dynamic brain communications characterized by both fast and slow features.
- **Two Brain Regions** Semedo et al. [2019]; Zandvakili & Kohn [2019]: Simultaneous spike train recordings from a monkey’s primary visual area (V1) and secondary visual cortex (V2), with a 6Hz drifting grating as the external stimulus.
- **Five Brain Regions** Siegle et al. [2021]: Simultaneous spike train recordings from a mouse’s primary visual cortex (VISp), rostralateral area (VISrl), anterolateral area (VISal), posteromedial area (VISpm), and anteromedial area (VISam), with a 4Hz drifting grating as the external stimulus.

Baselines. We compare our model with three methods:

- **DLAG** Gokcen et al. [2022]: A Gaussian Process Factor Analysis model with a MOSE kernel, designed for neural recordings from two brain regions. It can be used to learn both across-region and within-region latent communications.
- **mDLAG** Gokcen et al. [2024a]: An extension of DLAG that supports more than two brain regions with a different inference approach. Unlike DLAG, it assumes all latent variables correspond to across-region communications and does not explicitly model within-region dynamics.

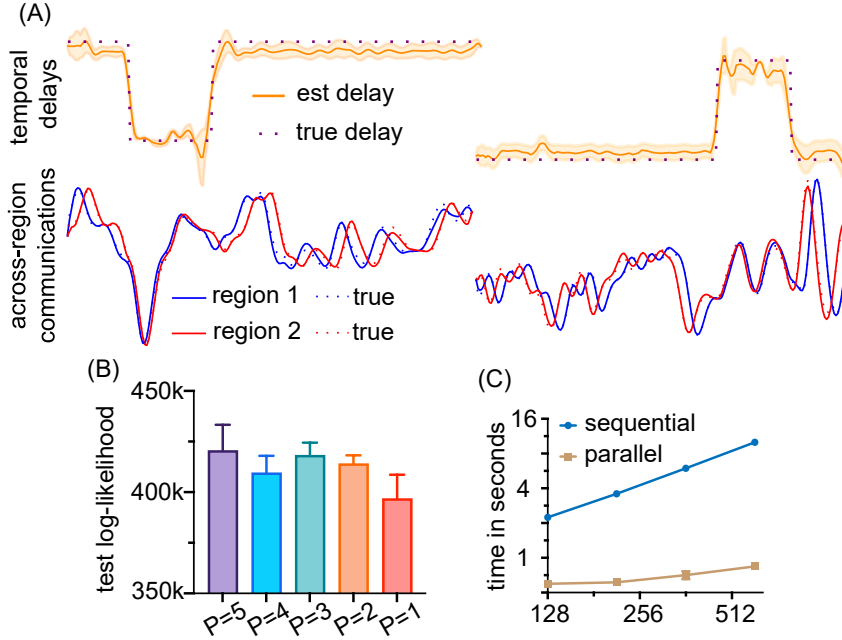


Figure 1: Evaluation of the ADM on synthetic brain communication data. (A) Estimated across-region communications, temporal delays, and ground truth over T bins for $P = 5$. The shaded area represents the variance of the estimated delay across five different runs. (B) Test log-likelihood summed over trials and time bins, showing that performance remains stable for different P . (C) Comparison of the time costs for the sequential and parallel scan-based Kalman EM with GPU parallelization, demonstrating that the parallel version is significantly faster, especially for larger T .

- **MRM-GP** [Li et al. \[2024\]](#): An approximation of a Gaussian Process with a Cross-Spectral Mixture (CSM) kernel [Ulrich et al. \[2015\]](#), formulated as an SSM with $O(T)$ complexity. It is designed to learn frequency-based communications between two brain regions and can capture both across-region and within-region latent dynamics.

Evaluation. We evaluate our model and baseline models by randomly splitting the data into training, validation, and testing sets with a ratio of 0.8, 0.1, and 0.1, respectively. Since all models assume a linear/Gaussian relationship between the latent variables and observed data, we assess their performance by computing the observation test log-likelihood: $\text{LL}(\mathbf{x}_{\text{test}}, \mathbf{y}_{\text{test}})$, where \mathbf{x}_{test} represents the inferred test latent variables, and \mathbf{y}_{test} denotes the test neural recordings. To mitigate randomness, we report the average test log-likelihood over five different random seeds.

4.1 Synthetic Data

In this section, we simulate a common phenomenon in neuroscience where brain region communications are dynamic [Parra & Tobar \[2017\]](#). Our goal is to evaluate our model's ability to recover time-varying temporal delays and latent variables.

Experimental setup. We generate 120 independent trials for two brain regions ($N = 2$) with an order of $P = 5$ and $T = 200$ time bins. Each region contains 50 neurons, with $m_a = 2$ groups of across-region communications and $m_w = 1$ group of within-region variables. For across-region communications, the first group represents forward communication, characterized by a larger positive delay of 5 bins and a smaller positive delay of 1 bin during time bins 30 to 70. The second group represents feedback communication, with a larger negative delay of -5 bins and a smaller negative delay of -1 bin during time bins 130 to 170. For across-region and within-region dynamics, the length scales are set to $l = 5$ and $l = 2.5$, respectively.

Note that large delays in this context are intended to represent slow communication in the brain, whereas an extremely large delay would imply an absence of communication between regions. A

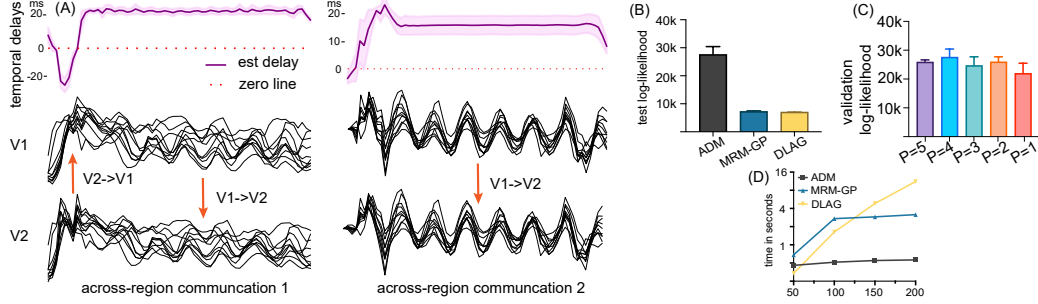


Figure 2: Evaluation of the ADM on spike trains from V1 and V2. (A) Estimated across-region communications and time-varying temporal delays from the test dataset (ten trials are shown), showing a shift from slow feedback and forward communication (larger delays) to dominant fast forward communication (smaller delays) over time. (B) Test log-likelihood comparison, where ADM outperforms MRM-GP and DLAG by capturing continuously time-varying temporal delays. (C) Validation log-likelihood across different P values. (D) Computational time comparison, demonstrating ADM’s efficiency through parallel computation, outperforming MRM-GP and DLAG.

small delay indicates fast communication. Therefore, our data simulation is designed to reflect a scenario where region A initially has minimal effective communication with region B (delay of 5), then suddenly transmits a signal (delay of 1), followed by another period of ineffective communication (delay of 5). A delay of -5 represents communication in the opposite direction. During fitting, we set $m_a = 2$, $m_w = 1$, and $P = 5$.

Results. Figure 1(A) presents the estimated and truth across-region communications, temporal delays, and ground truth over T bins for $P = 5$. For the estimated delay, the shaded area represents the variance across five different runs. Our model effectively captures time-varying communications for both latent dynamics and delay. See Appendix E for within-region neural activities.

Figure 1(B) shows the test log-likelihood summed over trials and time bins. The results indicate that performance remains relatively stable for $P \in [2, 5]$, except for $P = 1$, which yields the lowest performance.

Figure 1(C) compares the time costs of the sequential and parallel scan-based Kalman EM algorithms with GPU parallelization. We generate synthetic data with up to $T = 600$ time bins. The results demonstrate that the parallel version is significantly faster than the sequential update.

4.2 Two Brain Regions

In this section, we investigate the interactions between the mouse’s primary visual area (V1) and secondary visual cortex (V2) in response to a 6Hz drifting grating. Additionally, we compare our model’s performance and inference time with MRM-GP and DLAG.

Experimental setup. We use smoothed multi-region spike trains from session 106r001p26 with an orientation of 0° . This dataset consists of 400 trials, each containing 64 time bins (20 ms per bin), with 72 V1 neurons and 22 V2 neurons. The monkey begins receiving the visual stimulus (drifting gratings) at the first time bin, and the stimulus persists throughout all 64 time bins. The number of across-region and within-region latent dynamics follows previous works Gokcen et al. [2022]; Li et al. [2024], where $m_a = 2$ and $m_w = 2$. The order $P = 4$ is selected based on performance evaluation on the validation dataset.

Results. Figure 2(A) presents the estimated across-region communications and time-varying temporal delays from the test dataset (showing ten trials, see Appendix E for within-region dynamics). Both groups of across-region communications exhibit a periodic pattern driven by the external drifting grating stimulus. Our model reveals a slow forward and feedback communication circuit (characterized by larger delays) between V1 and V2 immediately after stimulus onset. Over time, this shifts to a dominance of faster forward communication (with smaller delays). The time-varying temporal delays can be interpreted as follows: shortly after stimulus presentation, V1 triggers oscillatory dynamics

in V2, which in turn generates a strong feedback signal from V2 to V1, potentially reflecting the emergence of surprise or prediction error [Rao & Ballard \[1999\]](#). Subsequently, both regions begin to oscillate synchronously with dominant forward communication. Our findings on V1-V2 interactions align with previous studies [Gokcen et al. \[2022\]](#); [Li et al. \[2024\]](#); [Gokcen et al. \[2024a\]](#).

Figure 2(B) compares the test log-likelihood summed over trials and time bins, showing that our model, ADM, outperforms MRM-GP and DLAG, attributed to its ability to capture continuously time-varying temporal delays. Figure 2(C) presents the validation log-likelihood across different P values, with $P = 4$ achieving the highest value. Combined with the insights from Figures 2(A–B), this suggests that a small P value can effectively estimate model parameters and latent variables.

Figure 2(D) compares the computational time of our model with MRM-GP and DLAG on spike trains of varying T , obtained by concatenating trials. The use of parallel computation significantly improves efficiency, outperforming the linear model (MRM-GP) and the cubic model (DLAG).

4.3 Five Brain Regions

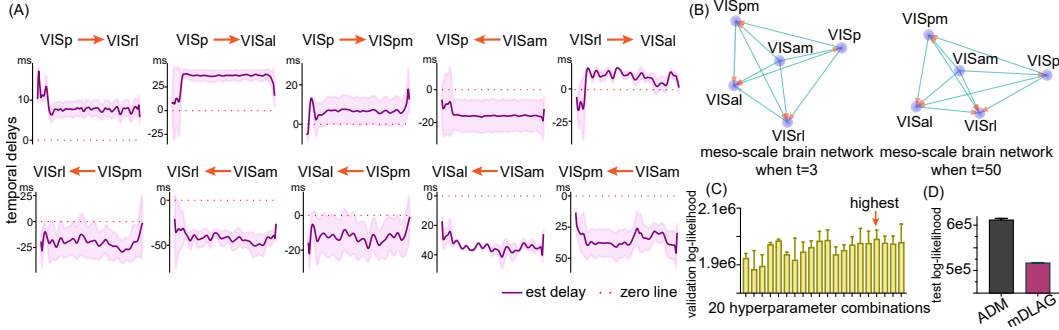


Figure 3: Evaluation of the ADM on spike trains from five visual brain regions. (A) Estimated pairwise temporal delays from one group of across-region communications, showing time-varying dynamics and alignment with the anatomical hierarchy of the mouse visual cortex. (B) Meso-scale brain networks at $t = 3$ and $t = 50$ time bins, illustrating changes in communication speed and direction. (C) Cross-validation results for hyperparameter selection, with $m_a = 3$, $m_w = 1$, and $P = 2$ achieving the highest validation log-likelihood. (D) Test log-likelihood comparison between ADM and mDLAG, demonstrating ADM’s superior fit due to its ability to model time-varying communications.

In this section, we scale up our model to a larger neural recording spanning five regions with increased time resolution. Our objective is to investigate across-region communications and identify the time-varying meso-scale brain network, defined as the dynamic network spanning sub-brain regions, e.g., regions in visual cortex.

Experimental setup. We use smoothed multi-region spike train data from the Visual Coding – Neuropixels project by the Allen Institute [Siegle et al. \[2021\]](#), specifically from session 750749662. This dataset includes spike trains recorded from VISp, VISrl, VISal, VISpm, and VISam—sub-areas of the mouse visual cortex. It consists of 120 trials, $T = 200$ time bins (each 10 ms), and a total of 202 neurons, with external visual stimuli comprising 4 Hz drifting gratings. Following the approach in [Gokcen et al. \[2022\]](#), we first apply Factor Analysis to estimate the total number of across-region and within-region latent dynamics, determining $M = 4$ (see Appendix F for details). We then conduct a grid search with 5-fold cross-validation to refine the number of across-region and within-region latent dynamics and the model order P , yielding $m_a = 3$, $m_w = 1$, and $P = 2$.

Results. Figure 3(A) presents the ten estimated pairwise temporal delays from one group of across-region communications. For the remaining groups and estimated latent dynamics, see Appendix E. Our results reveal consistent forward communication from VISp to downstream visual areas, such as VISrl, VISal, and VISpm, aligning with the known anatomical hierarchy of the mouse visual cortex [Siegle et al. \[2021\]](#). Additionally, these forward communications exhibit time-varying dynamics. For instance, communication between VISp and VISrl transitions from slow to fast, indicating an

enhanced interaction that gradually becomes more synchronous following the initial surprise response to the visual stimulus onset. In contrast, the communication between VISp and VISal shifts from fast to slow, suggesting inhibition induced by the external stimulus. Furthermore, our findings indicate that all communications involving VISam are feedback signals. This is expected, as VISam is positioned at the end of the anatomical hierarchy of the mouse visual system, consistent with the anatomical hierarchy scores reported in [Siegle et al. \[2021\]](#).

Figure 3(B) illustrates the corresponding meso-scale brain network based on the estimated temporal delays. Each node represents a region in the visual system, while directed edges indicate the directional communications. The length of each edge is determined by the estimated delays, reflecting the speed of communication. The figure presents two meso-scale brain networks at $t = 3$ and $t = 50$ time bins. The primary differences between these networks include changes in the speed of certain forward communications and a shift in the communication direction between VISrl and VISal, suggesting the emergence of gradually synchronous interactions following stimulus presentation.

Figure 3(C) presents the cross-validation results for twenty hyperparameter combinations. We first determine $M = 4$ using Factor Analysis (see Appendix F for details), then conduct a grid search over all combinations of $m_a \in [0, 4]$, $m_w \in [0, 4]$, and $P \in [2, 5]$. The highest validation log-likelihood is achieved with $m_a = 3$, $m_w = 1$, and $P = 2$.

Figure 3(D) compares the test log-likelihood, summed over trials and time bins, between our model (ADM) and mDLAG, which is an extension of DLAG that supports more than two brain regions using a variational inference method. The results indicate that ADM provides a better fit to the data, attributed to its ability to model time-varying communications. We do not compare MRM-GP and DLAG since they are limited to two brain regions. Additionally, we skip a time cost comparison with mDLAG because it is implemented only in MATLAB, which is significantly slower (taking hours to run) than our GPU-optimized implementation.

5 Discussion

Summary. Our findings highlight the importance of modeling time-varying multi-region neural communications and demonstrate that the Adaptive Delay Model (ADM) effectively captures these dynamics while maintaining computational efficiency. Existing methods for studying across-region neural interactions can be broadly categorized into non-delay models and delay models. While non-delay models provide directional communication patterns, they fail to capture temporal delays, limiting their ability to infer the communication speed. Conversely, delay models, such as DLAG and MRM-GP, introduce delay estimation but assume static or discretely changing delays, which do not reflect the continuously evolving nature of brain communications. Our results show that ADM overcomes these limitations by incorporating a flexible, time-varying delay mechanism, enabling a more biologically relevant representation of neural interactions.

Neuroscience Implications. Our results from large-scale neural recordings show that across-region communication delays are not static but change over time. Notably, we observe transitions from slow feedback and forward communication to fast forward interactions in both datasets (Section 4.2 and Section 4.3), aligning with adaptive sensory processing in the visual cortex. These findings show the importance of time-varying models in capturing the dynamic nature of brain communications.

Computational Advancements. Beyond its neuroscientific implications, our model contributes to the broader field of computational modeling by bridging temporally stationary GPs with SSMs. Traditional GP-SSM connections often rely on separability assumptions in spatial and temporal kernels, limiting their flexibility. Our proposed universal connection between arbitrary temporally stationary GPs and SSMs removes this restriction. Furthermore, by leveraging parallel scan algorithms, ADM achieves an impressive computational complexity of $O(\log T)$, significantly improving scalability compared to existing methods.

Limitations and Future Directions. Our model has a cubic time complexity with respect to the number of brain regions N and the SSM order P . Although these values are typically much smaller than T , they can still become computational bottlenecks for specific cases. A potential solution may involve leveraging frequency domain techniques. [Parnichkun et al. \[2024\]](#) proposed a state-free SSM with a controllable canonical transition matrix, similar to ours in Eq. 11, and utilized the Fast Fourier

Transform to achieve linear scaling in latent size. Similarly, Gokcen et al. [2024b] approximated the GP kernel in the frequency domain to reduce the computational cost to linear in latent size.

References

Blelloch, G. E. Prefix sums and their applications. 1990.

Boots, B. Learning stable linear dynamical systems. *Online]. Avail.: https://www.ml.cmu.edu/research/dap-papers/dap_boots.pdf [Accessed 30 05 2016]*, 2009.

Glaser, J., Whiteway, M., Cunningham, J. P., Paninski, L., and Linderman, S. Recurrent switching dynamical systems models for multiple interacting neural populations. *Advances in neural information processing systems*, 33:14867–14878, 2020.

Gokcen, E., Jasper, A. I., Semedo, J. D., Zandvakili, A., Kohn, A., Machens, C. K., and Yu, B. M. Disentangling the flow of signals between populations of neurons. *Nature Computational Science*, 2(8):512–525, 2022.

Gokcen, E., Jasper, A., Xu, A., Kohn, A., Machens, C. K., and Yu, B. M. Uncovering motifs of concurrent signaling across multiple neuronal populations. *Advances in Neural Information Processing Systems*, 36, 2024a.

Gokcen, E., Jasper, A. I., Kohn, A., Machens, C. K., and Yu, B. M. Fast multi-group gaussian process factor models. *arXiv preprint arXiv:2412.16773*, 2024b.

Grewal, M. S. and Andrews, A. P. *Kalman filtering: Theory and Practice with MATLAB*. John Wiley & Sons, 2014.

Karniol-Tambour, O., Zoltowski, D. M., Diamanti, E. M., Pinto, L., Brody, C. D., Tank, D. W., and Pillow, J. W. Modeling state-dependent communication between brain regions with switching non-linear dynamical systems. In *The Twelfth International Conference on Learning Representations*.

Li, W., Li, C., Wang, Y., and Wu, A. Multi-region markovian gaussian process: An efficient method to discover directional communications across multiple brain regions. In *Forty-first International Conference on Machine Learning*, 2024.

Lillicrap, T. P., Santoro, A., Marris, L., Akerman, C. J., and Hinton, G. Backpropagation and the brain. *Nature Reviews Neuroscience*, 21(6):335–346, 2020.

Loper, J., Blei, D., Cunningham, J. P., and Paninski, L. A general linear-time inference method for gaussian processes on one dimension. *Journal of Machine Learning Research*, 22(234):1–36, 2021.

Neumaier, A. and Schneider, T. Estimation of parameters and eigenmodes of multivariate autoregressive models. *ACM Transactions on Mathematical Software (TOMS)*, 27(1):27–57, 2001.

Parnichkun, R. N., Massaroli, S., Moro, A., Smith, J. T., Hasani, R., Lechner, M., An, Q., Ré, C., Asama, H., Ermon, S., et al. State-free inference of state-space models: The transfer function approach. *arXiv preprint arXiv:2405.06147*, 2024.

Parra, G. and Tobar, F. Spectral mixture kernels for multi-output gaussian processes. *Advances in Neural Information Processing Systems*, 30, 2017.

Rao, R. P. and Ballard, D. H. Predictive coding in the visual cortex: a functional interpretation of some extra-classical receptive-field effects. *Nature neuroscience*, 2(1):79–87, 1999.

Särkkä, S. and García-Fernández, Á. F. Temporal parallelization of bayesian smoothers. *IEEE Transactions on Automatic Control*, 66(1):299–306, 2020.

Semedo, J. D., Zandvakili, A., Machens, C. K., Byron, M. Y., and Kohn, A. Cortical areas interact through a communication subspace. *Neuron*, 102(1):249–259, 2019.

Siegle, J. H., Jia, X., Durand, S., Gale, S., Bennett, C., Graddis, N., Heller, G., Ramirez, T. K., Choi, H., Luviano, J. A., et al. Survey of spiking in the mouse visual system reveals functional hierarchy. *Nature*, 592(7852):86–92, 2021.

Solin, A. et al. Stochastic differential equation methods for spatio-temporal gaussian process regression. 2016.

Steinmetz, N. A., Aydin, C., Lebedeva, A., Okun, M., Pachitariu, M., Bauza, M., Beau, M., Bhagat, J., Böhm, C., Broux, M., et al. Neuropixels 2.0: A miniaturized high-density probe for stable, long-term brain recordings. *Science*, 372(6539):eabf4588, 2021.

Ulrich, K. R., Carlson, D. E., Dzirasa, K., and Carin, L. Gp kernels for cross-spectrum analysis. *Advances in neural information processing systems*, 28, 2015.

Wilson, A. and Adams, R. Gaussian process kernels for pattern discovery and extrapolation. In *International conference on machine learning*, pp. 1067–1075. PMLR, 2013.

Zandvakili, A. and Kohn, A. Paired v1-v2 neuronal spiking responses in anesthetized macaque monkey. *CRCNS.org*, 2019.

Zhao, Z. State-space deep gaussian processes with applications. *arXiv preprint arXiv:2111.12604*, 2021.

A Derivation for $\mathbf{V}\mathbf{V}^\top$, $\mathbf{W}\mathbf{V}^\top$, and $\mathbf{W}\mathbf{W}^\top$

Let's inspect $\mathbf{V}\mathbf{V}^\top \in \mathbb{R}^{NP \times NP}$ first. We have:

$$\begin{aligned} \mathbf{V}\mathbf{V}^\top &= \begin{bmatrix} x_1 & x_2 & \dots & x_{T-P} \\ x_2 & x_3 & \dots & x_{T-P+1} \\ \vdots & \vdots & \ddots & \vdots \\ x_P & x_{P+1} & \dots & x_{T-1} \end{bmatrix} \begin{bmatrix} x_1^\top & x_2^\top & \dots & x_P^\top \\ x_2^\top & x_3^\top & \dots & x_{P+1}^\top \\ \vdots & \vdots & \ddots & \vdots \\ x_{T-P}^\top & x_{T-P+1}^\top & \dots & x_{T-1}^\top \end{bmatrix} \\ &= \begin{bmatrix} x_1 x_1^\top + \dots + x_{T-P} x_{T-P}^\top & \dots & x_1 x_P^\top + x_2 x_{P+1}^\top + \dots + x_{T-P} x_{T-1}^\top \\ \vdots & \ddots & \vdots \\ x_P x_1^\top + \dots + x_{T-1} x_{T-P}^\top & \dots & x_P x_P^\top + x_{P+1} x_{P+1}^\top + \dots + x_{T-1} x_{T-1}^\top \end{bmatrix}, \end{aligned} \quad (15)$$

where the first element $x_1 x_1^\top \in \mathbb{R}^{N \times N}$ represents the auto-covariance of x_1 , which is essentially the kernel $\mathbf{K}(0)$ (Eq. 4). In other words, since \mathbf{x} is modeled as a stationary GP, the elements $x_1 x_1^\top, \dots, x_{T-1} x_{T-1}^\top$ are all equivalent and correspond to the diagonal elements $\mathbf{K}(0)$ in Eq. 4. Similarly, the elements $x_P x_1^\top, \dots, x_{T-1} x_{T-P}^\top$ represent cross-covariances with time interval $P-1$, which correspond to the off-diagonal elements $\mathbf{K}(P-1)$. Therefore, we can further write Eq. 15 as:

$$\begin{aligned} \mathbf{V}\mathbf{V}^\top &= \begin{bmatrix} \mathbf{K}(0) + \dots + \mathbf{K}(0) & \dots & \mathbf{K}(-P+1) + \dots + \mathbf{K}(-P+1) \\ \vdots & \ddots & \vdots \\ \mathbf{K}(P-1) + \dots + \mathbf{K}(P-1) & \dots & \mathbf{K}(0) + \dots + \mathbf{K}(0) \end{bmatrix} \\ &\propto \begin{bmatrix} \mathbf{K}(0) & \mathbf{K}(-1) & \dots & \mathbf{K}(-P+1) \\ \mathbf{K}(1) & \mathbf{K}(0) & \dots & \mathbf{K}(-P+2) \\ \vdots & \vdots & \ddots & \vdots \\ \mathbf{K}(P-1) & \mathbf{K}(P-2) & \dots & \mathbf{K}(0) \end{bmatrix}. \end{aligned} \quad (16)$$

Following the same way, we can also represent $\mathbf{W}\mathbf{V}^\top \in \mathbb{R}^{N \times NP}$ and $\mathbf{W}\mathbf{W}^\top \in \mathbb{R}^{N \times N}$ using \mathbf{K} :

$$\begin{aligned} \mathbf{W}\mathbf{V}^\top &\propto [\mathbf{K}(P) \ \mathbf{K}(P-1) \ \dots \ \mathbf{K}(1)], \\ \mathbf{W}\mathbf{W}^\top &\propto \mathbf{K}(0). \end{aligned} \quad (17)$$

If the computation of \mathbf{G} in Eq. 8 leads to numerical issues because $\mathbf{V}\mathbf{V}^\top$ has singular values that are nearly zero, a more numerically stable approach is to rewrite $\mathbf{V}\mathbf{V}^\top$ by Cholesky factorization:

$$\mathbf{D} = \begin{bmatrix} \mathbf{V}\mathbf{V}^\top & \mathbf{V}\mathbf{W}^\top \\ \mathbf{W}\mathbf{V}^\top & \mathbf{W}\mathbf{W}^\top \end{bmatrix} = \mathbf{L}\mathbf{L}^\top, \quad \mathbf{L} = \begin{bmatrix} \mathbf{L}_1 & 0 \\ \mathbf{L}_2 & \mathbf{L}_3 \end{bmatrix}, \quad \mathbf{V}\mathbf{V}^\top = \mathbf{L}_1 \mathbf{L}_1^\top, \quad (18)$$

where $\mathbf{D} \in \mathbb{R}^{N(P+1) \times N(P+1)}$, $\mathbf{W}\mathbf{V}^\top = \mathbf{L}_2 \mathbf{L}_1^\top$, $\mathbf{W}\mathbf{W}^\top \propto \mathbf{K}(0)$, and $\mathbf{L}_1 \in \mathbb{R}^{NP \times NP}$, $\mathbf{L}_2 \in \mathbb{R}^{N \times NP}$, $\mathbf{L}_3 \in \mathbb{R}^{N \times N}$ are the sub-matrices of \mathbf{L} . In practice, Eq. 18 factorizes $\mathbf{D} + \delta \mathbf{I}$ with a small positive number δ to ensure the positive definite of \mathbf{D} . Then, the estimation for \mathbf{G} can be cast in the form of \mathbf{L} and the measurement matrix \mathbf{Q} is the residual covariance of residual \mathbf{R} :

$$\begin{aligned} \hat{\mathbf{G}} &= \mathbf{W}\mathbf{V}^\top (\mathbf{V}\mathbf{V}^\top)^{-1} = \mathbf{L}_2 \mathbf{L}_1^{-1}, \\ \hat{\mathbf{Q}} &= \frac{(\mathbf{W} - \hat{\mathbf{G}}\mathbf{V})(\mathbf{W} - \hat{\mathbf{G}}\mathbf{V})^\top}{T - P - 1} = \frac{\mathbf{L}_3 \mathbf{L}_3^\top}{T - P - 1}. \end{aligned} \quad (19)$$

B Details for Kalman EM

In E-step, we have the expected log-likelihood as:

$$\begin{aligned}
Q(\Theta|\Theta^k) &= \mathbb{E}_{\mathbf{x} \sim p(\cdot|\mathbf{y}, \Theta^k)} [LL(\mathbf{x}, \mathbf{y}|\Theta)], \\
&\propto -\frac{1}{2} \sum_t (y_t^\top \mathbf{C}^{-1} y_t - 2y_t^\top \mathbf{C}^{-1} \mathbf{H} \mathbb{E}[x_t|\mathbf{y}, \Theta^k] + \mathbb{E}[x_t^\top \mathbf{H}^\top \mathbf{C}^{-1} \mathbf{H} x_t|\mathbf{y}, \Theta^k]) \\
&\quad - \frac{1}{2} \sum_t (\mathbb{E}[x_t^\top \hat{\mathbf{Q}}^{-1} x_t|\mathbf{y}, \Theta^k] - 2\mathbb{E}[x_t^\top \hat{\mathbf{Q}}^{-1} \hat{\mathbf{A}} x_{t-1}|\mathbf{y}, \Theta^k] \\
&\quad + \mathbb{E}[x_{t-1}^\top \hat{\mathbf{A}}^\top \hat{\mathbf{Q}}^{-1} \hat{\mathbf{A}} x_{t-1}|\mathbf{y}, \Theta^k]) - \frac{T}{2} \log(|\mathbf{C}|) - \frac{1}{2} \log(|\hat{\mathbf{Q}}|), \tag{20}
\end{aligned}$$

where all expectations $\mathbb{E}[\cdot]$ mentioned above are based on $\mathbb{E}[x_t|\mathbf{y}]$, $\mathbb{E}[x_t^\top x_t|\mathbf{y}]$, and $\mathbb{E}[x_t^\top x_{t-1}|\mathbf{y}]$, which are calculated through forward and backward passes known as Kalman Filter and Kalman Smoother [Boots \[2009\]](#), respectively. Specifically, if denoting $\tilde{x}_t = \mathbb{E}[x_t|\mathbf{y}]$, $\mathbf{C}_t = \mathbb{E}[x_t^\top x_t|\mathbf{y}]$, and $\mathbf{C}_{t,t-1} = \mathbb{E}[x_t^\top x_{t-1}|\mathbf{y}]$, we have:

$$\begin{aligned}
\mathbb{E}[x_t|\mathbf{y}, \Theta^k] &= \tilde{x}_t, \\
\mathbb{E}[x_t^\top \mathbf{H}^\top \mathbf{C}^{-1} \mathbf{H} x_t|\mathbf{y}, \Theta^k] &= \tilde{x}_t^\top \mathbf{H}^\top \mathbf{C}^{-1} \mathbf{H} \tilde{x}_t + \text{Tr}(\mathbf{H}^\top \mathbf{C}^{-1} \mathbf{H} \mathbf{C}_t), \\
\mathbb{E}[x_t^\top \hat{\mathbf{Q}}^{-1} x_t|\mathbf{y}, \Theta^k] &= \tilde{x}_t^\top \hat{\mathbf{Q}}^{-1} \tilde{x}_t + \text{Tr}(\hat{\mathbf{Q}}^{-1} \mathbf{C}_t), \tag{21} \\
\mathbb{E}[x_t^\top \hat{\mathbf{Q}}^{-1} \hat{\mathbf{A}} x_{t-1}|\mathbf{y}, \Theta^k] &= \tilde{x}_t^\top \hat{\mathbf{Q}}^{-1} \hat{\mathbf{A}} \tilde{x}_{t-1} + \text{Tr}(\hat{\mathbf{Q}}^{-1} \hat{\mathbf{A}} \mathbf{C}_{t,t-1}^\top), \\
\mathbb{E}[x_{t-1}^\top \hat{\mathbf{A}}^\top \hat{\mathbf{Q}}^{-1} \hat{\mathbf{A}} x_{t-1}|\mathbf{y}, \Theta^k] &= \tilde{x}_{t-1}^\top \hat{\mathbf{A}}^\top \hat{\mathbf{Q}}^{-1} \hat{\mathbf{A}} \tilde{x}_{t-1} + \text{Tr}(\hat{\mathbf{A}}^\top \hat{\mathbf{Q}}^{-1} \hat{\mathbf{A}} \mathbf{C}_t).
\end{aligned}$$

Then, in M-step, we aim to update the kernel parameters such that $Q(\Theta|\Theta^k)$ is maximized:

$$\Theta^{k+1} = \arg \max_{\Theta} Q(\Theta|\Theta^k). \tag{22}$$

C Generation Samples

To better understand the effect of different P values, we generate samples with $T = 200$ time bins from our model using various P values. Figure 4 shows that when P is very small (e.g., $P = 1$), the generated samples appear unsMOOTH. However, for $P \geq 2$, the generated samples exhibit no noticeable visual differences.

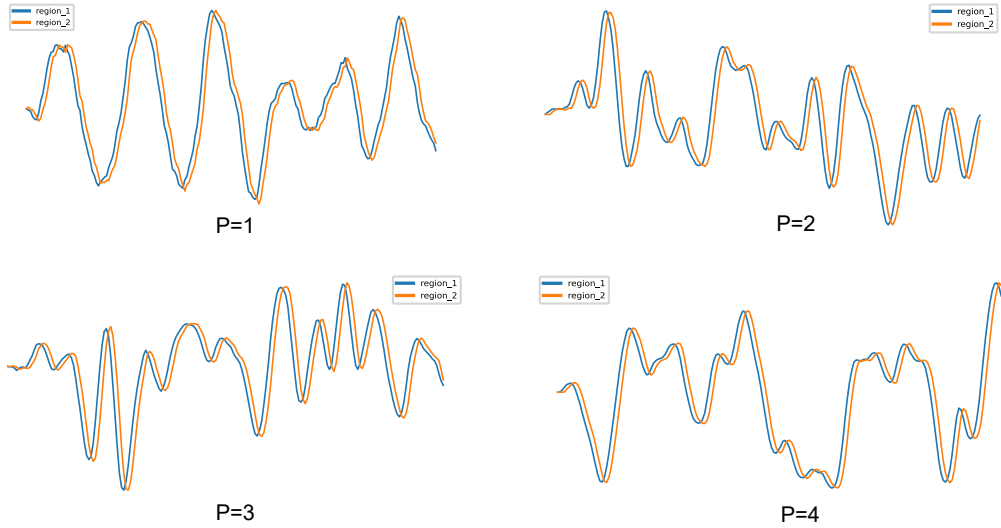


Figure 4: Generated samples from our model with MOSE kernel when $P = 1, 2, 3, 4$.

Table 1: MSE for GP regression with single-output kernels.

Reg-MSE / 10^{-1}	Exp	Matern 3/2	SE	RQ	SM
GP	5.7 ± 0.1	5.9 ± 0.2	3.1 ± 0.1	3.0 ± 0.1	3.0 ± 0.2
SSM-Approx	5.9 ± 0.1	6.2 ± 0.1	3.3 ± 0.1	3.4 ± 0.1	3.3 ± 0.2

Table 2: MSE for GP regression with multi-output kernels.

Reg-MSE / 10^{-1}	MOSE	MOSM	CSM	LMC
GP	7.4 ± 0.02	7.5 ± 0.02	8.2 ± 0.05	0.66 ± 0.02
SSM-Approx	7.6 ± 0.04	7.9 ± 0.08	7.7 ± 0.09	0.72 ± 0.02

D Gaussian Process Regression

To verify the universal connection between arbitrary temporally stationary Gaussian Processes (GPs) and State Space Models (SSMs), we compare GP regression performance using our SSM approximation and the standard GP. We generate samples of 300 points from a GP with added Gaussian noise as regression data. The samples are then randomly split into training ($t_{\text{train}}, y_{\text{train}}$) and testing ($t_{\text{test}}, y_{\text{test}}$) sets, with 60% used for training and 40% for testing.

The kernels we evaluated are:

- **Exponential (Exp):** Single-output with $\mathbf{K}(t, t') = \sigma^2 \exp\left(-\frac{|t-t'|}{l}\right)$.
- **Matern 3/2 (Matern):** Single-output with $\mathbf{K}(t, t') = \sigma^2 \left(1 + \frac{\sqrt{3}|t-t'|}{l}\right) \exp\left(-\frac{\sqrt{3}|t-t'|}{l}\right)$.
- **Squared Exponential (SE):** Single-output with $\mathbf{K}(t, t') = \sigma^2 \exp\left(-\frac{(t-t')^2}{2l^2}\right)$.
- **Rational Quadratic (RQ):** Single-output with $\mathbf{K}(t, t') = \sigma^2 \left(1 + \frac{(t-t')^2}{2\alpha l^2}\right)^{-\alpha}$.
- **Spectral Mixture (SM) Wilson & Adams [2013]:** Single-output with $\mathbf{K}(t, t') = \sum_{q=1}^Q \sigma_q^2 \exp\left(-\frac{(t-t')^2}{2l_q^2}\right) \cos(\omega_q(t - t'))$.
- **Multi-Output Squared Exponential (MOSE) Gokcen et al. [2022]:** Multi-output with $\mathbf{K}_{ij}(t, t') = \sigma_{ij}^2 \exp\left(-\frac{(t-t'+\delta_{ij})^2}{2l_{ij}^2}\right)$.
- **Multi-Output Spectral Mixture (MOSM) Parra & Tobar [2017]:** Multi-output with $\mathbf{K}_{ij}(t, t') = \sum_{q=1}^Q \sigma_{ij,q}^2 \exp\left(-\frac{(t-t'+\delta_{ij,q})^2}{2l_{ij,q}^2}\right) \cos(\omega_{ij,q}(t - t') + \phi_{ij,q})$.
- **Cross-Spectral Mixture (CSM) Ulrich et al. [2015]:** Multi-output with $\mathbf{K}_{ij}(t, t') = \sum_{q=1}^Q \sum_{r=1}^R \sigma_{i,q}^r \sigma_{j,q}^r \exp\left(-\frac{(t-t')^2}{2l_{ij,q}^2}\right) \cos(\omega_{ij,q}(t - t') + \phi_{ij,q}^r)$.
- **Linear Model of Coregionalization (LMC):** Multi-output with $\mathbf{K}(t, t') = \sum_{q=1}^Q B_q \otimes k_q(t, t')$, where B_q is a coregionalization matrix and $k_q(t, t')$ is a single-output kernel.

The number of orders P for each kernels are as follows:

- **Exponential (Exp):** $P = 1$.
- **Matern 3/2 (Matern):** $P = 2$.
- **Squared Exponential (SE):** $P = 2$.
- **Rational Quadratic (RQ):** $P = 4$.
- **Spectral Mixture (SM):** $P = 2$.
- **Multi-Output Squared Exponential (MOSE):** $P = 2$.
- **Multi-Output Spectral Mixture (MOSM):** $P = 2$.
- **Cross-Spectral Mixture (CSM):** $P = 4$.
- **Linear Model of Coregionalization (LMC):** When $k_q(t, t')$ is SE kernel, $P = 2$.

The results are shown in Table 1 and Table 2, where our SSM approximation demonstrates regression performance comparable to GP in terms of MSE.

E Additional Across- and Within-Region Latent Variables

Figure 5 presents the within-region neural activity for both synthetic data and V1-V2 neural spike trains. Figure 6 displays the across- and within-region communications, neural activity, and the estimated temporal delays for the remaining two groups.

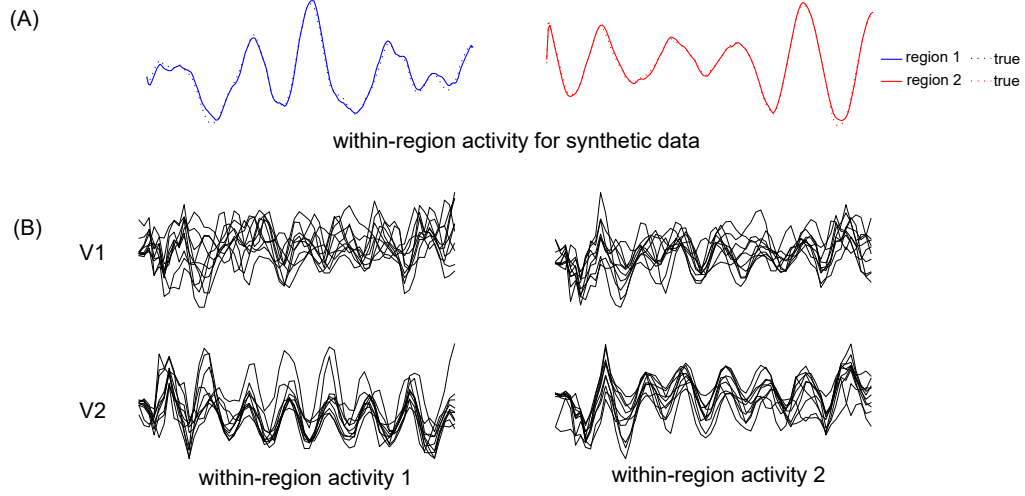


Figure 5: Within-region neural activity for both synthetic data and V1-V2 neural spike trains.

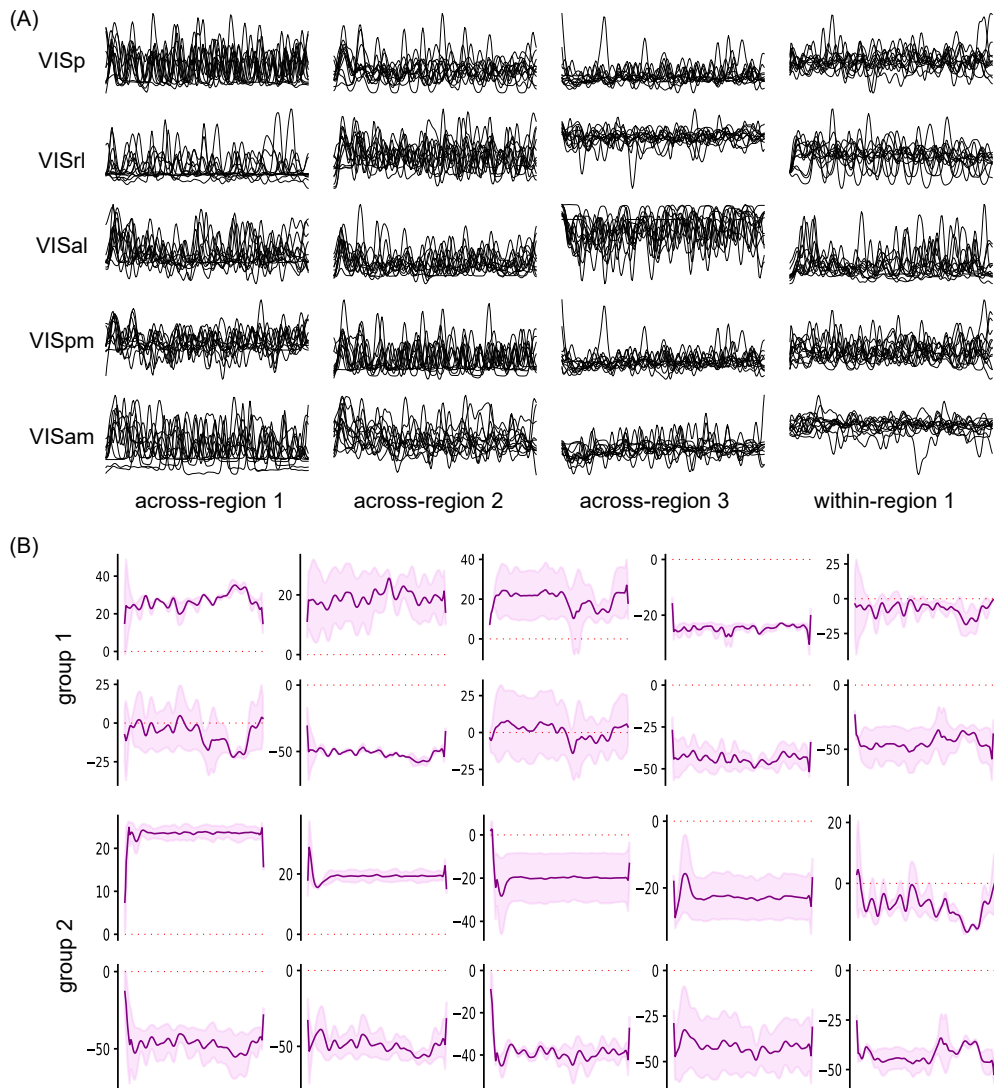


Figure 6: The across- and within-region communications, neural activity (ten trials are shown), and the estimated temporal delays for the remaining two groups.

F Factor Analysis for Five Regions Spike Trains

Figure 7 presents the Factor Analysis results for neural spike trains from five regions, and we select the latent size to be the largest optimal latent size across five regions, which is 4.

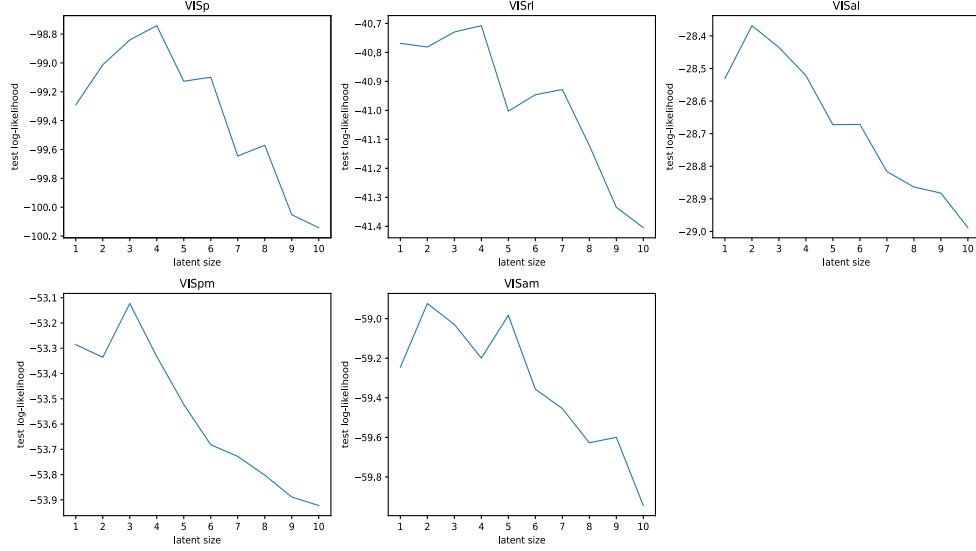


Figure 7: The figure presents Factor Analysis results for neural spike trains from five regions. The optimal latent size, determined as the maximum across all regions, is selected to be 4, yielding the highest test log-likelihood.